The density profile of the Milky Way's stellar halo out to 80 kpc

Xiang-Xiang Xue[1],Hans-Walter Rix[1],Zhibo Ma[2],Jo Bovy[3],Braimir Sesar[1]

ABSTRACT

We present the density profile of SEGUE-2 spectroscopic halo K giants by considering the selection function information. A sample of $\sim$ 2400 halo K giants up to 80 kpc from the Galactic center and its well-understood selection function enable us to get a robust measurement of the shape and radial profile of the Milky Way's stellar halo out to 80 kpc. The data show the stellar halo is oblate and its shape has strong dependence on metallicity (i.e. the more metal-poor stars show rounder density profile.). In addition, we find a strong evidence for variations in flattening with radius. After fitting the data to Einasto profile and a broken power-law with a constant halo flattening, we find the best-fitting Einasto profile with an effective radius at 21 kpc, a steepness index of 2.2, and a flattening (i.e. ratio of minor axis to major axis) of 0.78, and the best-fitting broken power-law with an inner slope of 2.7 and an outer slope of 4.2, together with a break radius at 30 kpc and a flattening of 0.78. These two best-fitting models are consistent within $1-\sigma$. Assuming the halo flattening varies with radii, the best-fitting Einasto profile has a smaller effective radius of 8 kpc, but a larger steepness index of 4.6, and the flattening changing from 0.5 at 10 kpc to 0.95 at 80 kpc. Furthermore, the Einasto profile with variable flattening is consistent with the density profiles with a constant flattening within $1-\sigma$.

Subject headings: galaxies: individual(Milky Way) – Galaxy: halo – Galaxy: stellar content – stars: K giants

1. Introduction

The Milky Way's stellar halo is an important diagnostic of the Galactic formation and the dynamics of the dark matter halo. The position-kinematics-abundance substructure in

[1]Max-Planck-Institute for Astronomy Königstuhl 17, D-69117, Heidelberg, Germany

[2]Department of Astronomy, Case Western Reserve University, Cleveland, OH 44106, USA

[3]Institute for Advanced Study, Einstein Drive, Princeton, NJ 08540, USA

the stellar halo is closely related to the formation mechanism of the Galaxy itself. While, Jeans (1915) equation is a robust method to determine the mass of Milky Way. Among the inputs of Jeans equation, the density profile of the stellar halo is one of the most imperative quantities. However, there is no consensus on the shape and radial profile of the stellar halo until now.

The most straightforward way to quantify the stellar halo distribution is star counts. However, this method requires large size and the completeness of the sample, so it is often applied to the photometric catalogs. Very early studies adopted star counts to analyze globular clusters(Harris 1976), RR Lyrae variables(Hawkins 1984; Wetterer & McGraw 1996), blue horizontal branch (BHB) stars(Sommer-Larsen 1987), combination of BHBs and RR Lyraes(Sluis & Arnold 1998), a star sample near the north galactic pole(Soubiran 1993), or K dwarfs(Gould et al. 1998), and found the stellar halo is well fitted by a single power-law ($\nu \approx (distance)^{-\alpha}$) with index α of $3 \sim 3.5$ and flattening of $0.5 \sim 1$. However, Saha (1985) found dozens of RR Lyraes are well described by a broken power-law with $\alpha \sim 3$ out to 25 kpc, and $\alpha \sim 5$ beyond 25 kpc.

All of above studies were based on a few hundred objects at most. Recent years, with the development of sky surveys, the sizes of the photometric samples expand more than 10 times. Robin et al. (2000) used a wide set of deep star counts in pencil-beam survey at high and intermediate galactic latitudes to model the density profile and found the best-fit density profile with a flattening of 0.76, a power index of 2.44. Siegel et al. (2002) found $70,000$ stars in seven Kapteyn selected areas are consistent with a power-law density with index of 2.75 and flattening of 0.6. De Propris et al. (2010) made use of BHB stars from the Two-degree Field Quasar Redshift Survey to find that the halo is almost spherical with a power-law index of $\alpha \sim 2.5$ out to ~ 100 kpc. Sesar et al. (2011) used $27,544$ near-turnoff main-sequence stars out to ~ 35 kpc selected from Canada-France-Hawaii Telescope Legacy Survey to find the flattening of stellar halo is 0.7 and the density distribution is consistent to a broken power low with an inner slope of 2.62 and an outer slope of 3.8 at the break radius of 28 kpc, or an equally good Einasto profile(Einasto & Haud 1989) with steepness index of 2.2 and effective radius of 22.2 kpc. Deason et al. (2011) analyzed $\sim 20,000$ A-type photometric stars selected from Sloan Digital Sky Survey data release 8(Ahn et al. 2012) and obtained the best-fitting broken power-law density with an inner slope of 2.3, and an outer slope of 4.6, with a break radius at 27 kpc and a constant flattening of 0.6. Straight after that, Deason et al. (2014) found a very steep outer halo profile with slope of 6 beyond 50 kpc, and even steeper slopes of $6 \sim 10$ at larger radii.

In addition, there are several pieces of work to detect variations in the flattening with radius. Preston et al. (1991) found the density distribution for RR Lyraes follow a power-law

with $\alpha \sim 3.2$, together with a variable flattening changing linearly from 0.54 at center to 1 at 20kpc. But, else work (Sluis & Arnold 1998; Sesar et al. 2011; Deason et al. 2011) found no evidence for a varying shape with radius.

The data sets with only photometric information are lack of metallicities, so the distances are less precise. Furthermore, it is hard to explore the metallicity dependence of the stellar halo's shape and radial profile. The spectroscopic data sets enable us to take advantage of metallicities and velocities, but the observed star counts do not reflect the underlying stellar distribution. Any spectroscopic observation suffers from the target selection criteria. Therefore, to derive the underlying density distribution, the selection function of the spectroscopic observation must be clearly understood. RR Lyraes and BHBs have long been used as tracers to study the halo density profile, because they have precise distances and are bright enough to be observed at radii out to ~ 100 kpc, but it is painstaking work to gather such data. Comparing to Main-sequence stars and K-giant stars, RR Lyraes and BHBs are less representative because they are very old and metal-poor population(Xue et al. 2011).

Xue et al. (2014) presents a catalog of K giants with unbiased distances, metallicities, velocities and photometric information, drawn from the Sloan Extension for Galactic Understanding and Exploration(Yanny et al. 2009, SEGUE), which contains ~ 300 stars beyond 50 kpc. For K giants observed in SEGUE-2, we can understand their selection function well, so it is possible for us to explore the density profile of halo K giants.

The goal of this paper is to describe radial stellar halo profile from $10 - 80$ kpc using parameterized models (i.e. Einasto profile and broken power-law), to explore the shape and its variation, and to explore metallicity dependence of the shape and radial profile of the stellar halo.

In the next section, we lay out the properties and the selection function of the SEGUE K giants. In §3, we present the method of fitting a series of parameterized models to SEGUE-2 K giants by considering the selection function. The results for the stellar halo profile and tests on the metallicity dependence of the shape and radial profile are presented in §4. Finally, §5 discusses the comparison between our results and previous work.

2. SEGUE-2 K giants and their selection function

2.1. Data

The Sloan Digital Sky Survey(SDSS; York et al. 2000) is an imaging and spectroscopic survey covering roughly a quarter of the sky, which has both *ugriz* imaging (Fukugita et al. 1996; Gunn et al. 1998; Stoughton et al. 2002; Pier et al. 2003; Eisenstein et al. 2011) and low resolution spectra ($\lambda/\Delta\lambda \sim 2000$). SEGUE is one of the key projects and has two phases named SEGUE-1 and SEGUE-2, which aim to explore the nature of stellar populations from 0.5 kpc to 100 kpc(Yanny et al. 2009, and Rockosi et al. in prep.). The original SEGUE-1 obtained spectra of 240,000 stars with g = 14 − 20 to investigate Milky Way structure, and SEGUE-2 spectroscopically observed around 120,000 stars, focusing on the in situ stellar halo of the Galaxy.

K giants are specially targetted in the SEGUE project. There are three sub-categories of K giants named "l-color K giants", "red K giants", and "proper-motion K giants". The l-color K-giant category uses l-color, a photometry metallicity indicator for stars in the color range $0.5 < (g-r)_0 < 0.8$, to select metal-poor K giants, which occupy about 90% of the K-giant sample. The target selection criteria changed a lot during the implementation of SEGUE-1, so the selection function of SEGUE-1 is fairly complicated. However, SEGUE-2 adopted an invariable color-magnitude cut to select K giants: $15.5 < g_0 < 18.5$, $r_0 > 15$, $0.7 < (u-g)_0 < 3$, $0.5 < (g-r)_0 < 0.8$, $0.1 < (r-i)_0 < 0.6$, and $l-color > 0.09$[1]. Therefore, in this work, we only correct the selection function of SEGUE-2 l-color K giants and use them to fit the halo density profile. To eliminate the contamination from disk component, we cull K giants with [Fe/H] > -1.2 and |z| < 4 kpc, which leads to a final sample of 2413 l-color K giants. Figure 1 show the sky coverage, the spatial distributions without accounting for the selection function and metallicity distribution along with the distances of the SEGUE-2 l-color K giants after eliminating disk component. The l-color K giants distribute in the pencil-beam on the sky as the nature of the SEGUE survey, and spread out from 7 kpc to 85 kpc far from the Galactic center. The mean metallicity of the l-color K giants is −1.75 dex, and some l-color K giants have metallicities as poor as −3.5.

To understand the underlying spatial distribution of the K giants, we need to correct the SEGUE-2 K-giant selection function, which reflects the relation between the stars with good enough spectra to classify a star as a giant and their photometric (volume-complete parent) population. Accounting for the pencil-beam nature of SEGUE survey, we will analyze the selection fraction plate by plate (see §2.2).

---

[1]https://www.sdss3.org/dr9/algorithms/segue_target_selection.php#S2_table.

2.2. The selection function of SEGUE-2 l-color K-type stars

Rix & Bovy (2013) claimed that spectroscopic surveys of the Milky Way are always affected by various selection effects, commonly referred to as "selection biases", which are due to a set of objective and repeatable decisions of what to observe (necessitated by the survey design). Bovy et al. (2012) corrected the selection function of the spectroscopic SEGUE G-dwarf sample. Similar to Bovy et al. (2012), we also want to derive the relation between the stars with successfully spectroscopic observations and their photometric population. We treat the spectra that have good Mg index and stellar atmospheric parameters determined by the SEGUE Stellar Parameter Pipeline(SSPP; Lee et al. 2008a,b, 2011), but have no strong G band, as successfully observed spectra, because these properties are necessary for giant classification. The spectrum is the sole tool to classify a star as a giant or not, so it is impossible to know which stars are giants in the photometric sample. Fortunately, the sample of SEGUE K-type stars was obtained by uniformly sampling in the extinction-corrected color-magnitude boxes so that the giants to non-giants ratio is consistent from photometric sample to spectroscopic sample. In this way, the selection function of K-type stars reflects directly that of K giants.

In the area of each SEGUE-2 plate, we select all potential targets that satisfy the selection criteria of SEGUE-2 l-color K giants and have good proper motion less than 11 masyr^{-1}. To infer the dependence on color and apparent magnitude of the selection function, we look at the distribution of the photometric K-giant candidates in color-magnitude space with the distribution of the successfully spectroscopic sample overlaid for all SEGUE-2 plates together. Figure 2 shows that the spectroscopic sampling is relatively fair in colors and magnitudes for l-color K-giant candidates.

Our model for the SEGUE-2 K-giant candidates selection function is independent on colors and magnitudes, but plate-dependent. For each plate we define the number of the "successful" spectroscopic K-giant targets as N_{sp}, and N_{ph} as the number of photometric K-giant targets. Thus, the plate-dependent selection function (shown as Figure 3) is given by

$$S(plate) \;=\; \frac{N_{sp}}{N_{ph}} \tag{1}$$

3. Density profile modeling approach

Due to the "selection biases" of the spectroscopic survey, the observed star counts of the spectroscopic sample can not reflect the underlying stellar distribution. Therefore, to explore

the underlying stellar distribution, we must account for 4 effects: (1) the plate-dependent selection fraction of stars with spectra (see Figures 2 and 3), (2) the photometric distances that depend on color and [Fe/H], (3) the priors of metallicities and luminosities, and (4) the pencil-beam nature of the SEGUE survey, shown as the sky map of l-color K giants in Figure1.

Followed Bovy et al. (2012) and Rix & Bovy (2013), we express below how to fit the density profile using maximum likelihood method, by taking all of above effects into account. Since we have good $\mathcal{DM}$ for the SEGUE K giants, we use $(\mathcal{DM}, M_r, [\mathrm{Fe/H}], l, b)$ as observables. To infer the spatial number density profile of K giants, we assume a density profile with parameters $\mathrm{p_H}$ as $\nu_\star(\mathcal{DM}, \mathrm{l, b|p_H})$, and generate the expected observed distribution of stars in the spectroscopic sample by accounting for the selection function, photometry-distance relation and priors of metallicities and luminosities, and then this predicted distribution is compared to the observed distribution of the sample to get the best-fit parameters. The explicit form of the expected rate function is

$$\begin{aligned}\lambda(\mathrm{M_r}, \mathcal{DM}, [\mathrm{Fe/H}], \mathrm{l, b|p_H}) &= |\mathrm{J(x, y, z; \mathcal{DM}, l, b)}| \times \nu_\star(\mathcal{DM}, \mathrm{l, b|p_H}) \times \mathrm{p(M_r)} \times \mathrm{p([Fe/H])} \\ &\quad \times \mathrm{S(l, b)} \times \mathrm{S(m(\mathcal{DM}, M_r), c(M_r, [Fe/H]))} \qquad (2)\end{aligned}$$

Here $(\mathcal{DM}, \mathrm{l, b})$ are equivalent to Heliocentric polar coordinates corresponding to rectangular coordinates $(\mathrm{X, Y, Z})$. The Jacobian term $|\mathrm{J(x, y, z; \mathcal{DM}, l, b)}|$ is to transform from $(\mathrm{X, Y, Z})$ to $(\mathcal{DM}, \mathrm{l, b})$ coordinate. Please note that the volume of each plate is independent on l and b, because all the SEGUE plates have the same solid angle of 7 deg^2. When analysing the data plate by plate, the Jacobian term should be $|\mathrm{J(x, y, z; \mathcal{DM})}|$. $\nu_\star(\mathcal{DM}, \mathrm{l, b|p_H})$ is the underlying spatial number density of l-color K giants (i.e. halo density profile). $\mathrm{p(M_r)}$ and $\mathrm{p([Fe/H])}$ are the priors of luminosity and metallicity. $\mathrm{S(l, b)} \times \mathrm{S(m, c)}$ is the selection function as given in Eq.(1). The explicit form for each term in Eq.(2) is expressed as below:

$$|\mathrm{J(x, y, z; \mathcal{DM})}|_{\mathrm{plate}} = \frac{d^3 \ln 10}{5} \times A_p, \qquad \text{where } \mathrm{A_p} = 7 \text{ deg}^2; \quad \mathrm{d} = 10^{\frac{\mathcal{DM}}{5} - 2} \text{ kpc}$$

$$\mathrm{p(M_r)} \propto \begin{cases} 10^{0.32\mathrm{M_r}}, & \text{if } \mathrm{M_{r\ min,obs}} < \mathrm{M_r} < \mathrm{M_{r\ max,obs}} \\ 0, & \text{otherwise} \end{cases}$$

$$\mathrm{p([Fe/H])} \propto \begin{cases} \mathrm{p([Fe/H])_{obs}}, & \text{if } [\mathrm{Fe/H}]_{\mathrm{min,obs}} < [\mathrm{Fe/H}] < [\mathrm{Fe/H}]_{\mathrm{max,obs}} \\ 0, & \text{otherwise} \end{cases}$$

$$S(l_{plate}, b_{plate}) = \begin{cases} \frac{N_{spec.}}{N_{phot.}}, & \text{if in plate} \\ 0, & \text{otherwise} \end{cases}$$

$$S(m(\mathcal{DM}, M_r), c(M_r, [Fe/H])) \propto \begin{cases} 1, & \text{if } m_{min,obs} < m < m_{max,obs} \text{ and } c_{min,obs} < c < c_{max,obs} \\ 0, & \text{otherwise} \end{cases}$$

As discussed in Bovy et al. (2012) the likelihood of the data given p_H, can be written as

$$\mathscr{L}\big(\mathrm{data_i}|\mathrm{p_H}\big) = \mathrm{c}_\lambda^{-\mathrm{N_{KG}}} \prod_{\mathrm{i}=1}^{\mathrm{N_{KG}}} \lambda(\mathrm{M_{ri}}, \mathcal{DM}_\mathrm{i}, [\mathrm{Fe/H}]_\mathrm{i}, \mathrm{l_i}, \mathrm{b_i}|\mathrm{p_H}) \tag{3}$$

where the normalization c_λ is the integral over the volume in $(\mathcal{DM}, l, b, M_r, [Fe/H])$ space.

$$\mathrm{c}_\lambda = \sum_{\mathrm{i}=1}^{\mathrm{N_{plate}}} \int\int\int \lambda(\mathrm{M_r}, \mathcal{DM}, [\mathrm{Fe/H}], \mathrm{l_{plate}}, \mathrm{b_{plate}}|\mathrm{p_H}) \mathrm{dM_r} \mathrm{d}\mathcal{DM} \mathrm{d}[\mathrm{Fe/H}] \tag{4}$$

Specifically, this normalization integral can be computed efficiently using Gaussian quadrature rule. We adopt 48 transformation points, and then the parameter-independent parts such as Jacobian term, priors of luminosity and metallicity and selection function can be pre-computed on a dense grid. Then we vary (grid or Markov chain) the p_H until we get a good solution. We use the Python package emcee(Foreman-Mackey et al. 2013) to do the model fitting.

4. Result

In this section, we present the results of applying the maximum-likelihood method described in §3 to the sample of SEGUE-2 l-color K giants. We adopt a set of popular density profiles with constant flattening, such as Einasto profile and broken power-law, and then we test the metallicity dependence of the shape and radial profile and the radial variations in shape.

4.1. Einasto profile

The Einasto profile(Einasto & Haud 1989) is a function that describes how the density distribution of a spherical system changes with distance, which has the same mathematical

form as Sérsic's law(Sérsic 1963). Generally speaking, the Sérsic's law is used to describe the 2D surface brightness (i.e. projected density) profile of galaxies, but Einasto profile is treated as a 3D density profile. The advantage of Einasto profile is to trace a variable fall-off distribution without using a break radius. Einasto profile has been used to describe many types of system, including galaxies(Einasto & Haud 1989), dark matter halos(Merritt et al. 2006; Graham et al. 2006; Navarro et al. 2010) and Galactic stellar halo(Sesar et al. 2011; Deason et al. 2011). We adopt a similar expression of Einasto profile as the definition in Merritt et al. (2006), but bring in the flattening q:

$$\nu_\star(\mathrm{r_q}) \;=\; \nu_0 \; exp\left\{-d_n\left[(r_q/r_{eff})^{1/n}-1\right]\right\} \tag{5}$$

where

$$\begin{aligned} \mathrm{r_q} &= \sqrt{x^2+y^2+z^2/q^2}, \text{ which can be calculated from } (\mathcal{DM}, l, b) \text{ and q} \\ \mathrm{d_n} &\approx 3n-1/3+0.0079/n, \text{ for } n \geq 0.5 \end{aligned}$$

The shape of the halo is described by the flattening q, and the radial density profile is characterized by the effective radius $\mathrm{r_{eff}}$ and steepness index n. The smaller n generates a density distribution with steeper outer profile. The term $\mathrm{d_n}$ is to make sure the mass within $\mathrm{r_{eff}}$ is half of the total mass. The $\mathrm{r_q}$ is the spatial radius accounting for the flattening.

We use the methodology described in §3 to fit the parameterized Einasto profile, and get the best-fitting Einasto profile with parameters $\mathrm{q} = 0.78 \pm 0.02$, $\mathrm{n} = 2.2 \pm 0.3$, and $\mathrm{r_{eff}} = 21 \pm 1$ kpc shown in Figure 4. To test how accurately our models represent the observed distance distribution of the data, we compare the predicted distance distribution by the best-fit model with the data. Figure 5 shows that the best-fit Einasto profile predicts a comparable distribution of distance moduli with the observation.

4.2. Broken power-law profile

Saha (1985) found different power-law index in and out 25 kpc based on dozens of RR Lyraes. Recent studies(Sesar et al. 2011; Deason et al. 2011, 2014) found the stellar halo also can be described well by a broken power-law. The broken power-law profile has been another equally good model to describe the density distribution of the stellar halo. It uses a discontinuous form to describe the variation of density distribution with distance by imposing a break radius. We define the broken power-law profile same as Deason et al. (2011):

$$\nu_\star\left(\mathrm{r_q}\right) = \begin{cases} \nu_0 \; \mathrm{r_q^{-\alpha_{in}}}, & \mathrm{r_q} \leq \mathrm{r_{break}} \\ \nu_0 \; \mathrm{r_{break}^{\alpha_{out}-\alpha_{in}}} \; \mathrm{r_q^{-\alpha_{out}}}, & \mathrm{r_q} > \mathrm{r_{break}} \end{cases} \tag{6}$$

Here r_q is an ellipsoidal distance with the same definition as that in Einasto profile. Figure 6 shows the l-color K giants fit well with a broken power-law with an inner slope of $\alpha_{in} = 2.7 \pm 0.1$ and an outer slope of $\alpha_{out} = 4.2 \pm 0.2$, breaking at $r_{break} = 30 \pm 3$ kpc, together with a flattening of $q = 0.78 \pm 0.02$. The flattening is consistent with that of the best-fit Einasto profile. The broken power-law profile also predicts a consistent $p(\mathcal{DM})$ to the observation (shown as Figure 5).

Deason et al. (2014) found the stellar halo drops a lot beyond 50 kpc, so we also use our data to fit triple power-laws with six free parameters (α_{inner}, α_{middle}, α_{outer}, r_{break1}, r_{break2}, q). Here, α_{inner}, α_{middle} and α_{outer} are the power indexes within r_{break1}, between r_{break1} and r_{break2}, and beyond r_{break2} respectively, and q is the flattening. However, we can not find the best-fit of the second break radius, which means no evidence of strong drop beyond 50 kpc. We find the best first break radius r_{break1} is at 30 kpc, the inner slope α_{inner} is 2.7, the middle slope is equal to the outer slope ($\alpha_{middle} = \alpha_{outer} = 4.2$), and the flattening q is still 0.78.

4.3. The metallicity dependence of the stellar halo's shape and radial profile

The shape of the stellar halo is to describe a halo is oblate ($q < 1$) or spherical ($q = 1$), so it is characterized by the flattening parameter. The radial profile of the stellar halo is to describe how steep the distribution is and where the slope begins to change, so the parameters n and r_{eff} of Einasto profile or the power-law index and break radius of broken power-law profile can be used to indicate the radial profile. In this section, we use Einasto profile only to test the metallicity dependence of flattening and radial profile.

To discuss the metallicity-dependence of the flattening and radial profile, we split the l-color K giants into three almost equal-size sub-samples according to the metallicities, and fit Einasto profile with fixed $n = 2.2$ to them to obtain the best-fit parameters q and r_{eff}. The equal-size samples enable to reach similar precision of model fitting. We find the distribution of less metal-poor stars ($q \sim 0.7$) appears flatter than that of more metal-poor stars ($q \sim 0.85$), but the three sub-samples have similar effective radii ($r_{eff} \sim 20$ kpc), shown as Figure 7. In other words, the shape of the stellar halo has strong metallicity-dependence, but the radial profile has no strong metallicity-dependence.

More metal-poor stars are very old, and likely to stay in distant halo, so we attribute the rounder shape of more metal-poor stars to the increase of the flattening with the distance. In next section, we will look into the variation of the flattening.

4.4. The variation of the flattening

Previous work found the evidence for the increase of flattening with radii(Preston et al. 1991). We also find strong metallicity-dependence on the flattening by fitting to the Einasto profile with a constant flattening as described in §4.3, which we attribute to the increase of the flattening with the distances. In order to see if we could find any evidence for the variation of flattening as a function of radii, we substitute the following three expressions for q(r):

$$q\,(r) = q_{inf} - (q_{inf} - q_0)\exp\left(1 - \frac{\sqrt{r^2 + r_0^2}}{r_0}\right) \tag{7}$$

$$q\,(r) = \sqrt{q_0^2 + (q_{inf}^2 + q_0^2)\,\frac{r^2}{r^2 + r_0^2}} \tag{8}$$

$$q\,(r) = q_0\sqrt{\frac{r^2 + r_0^2}{q_0^2 r^2 + r_0^2}} \tag{9}$$

where q_{inf} is the flattening at $r \to +\infty$, q_0 is the flattening at center, and r_0 is the scale radius, over which the change of flattening occurs. Equation (7) is our guess on the variation of flattening following an exponential distribution. Equation (8) is a Osipkov-Merritt(-like) flattening[need a reference, but I have not found it]. Equation (9) comes from Sluis & Arnold (1998), so we name it as Sluis-Arnold flattening. We fit Einasto models with above three forms of varying flattening to the data and find small scale radii are favored ($r_0 \sim 10$ kpc), with center flattening of about 0.3. Figure 5 shows all three best-fitting Einasto models with varying flattening fit well to the observation, and are undistinguishable. The best-fitting Einasto model with an exponential variation of flattening (Eqn. 7) has $q_{inf} = 0.9 \pm 0.04$, $q_0 = 0.3 \pm 0.1$, $r_0 = 8 \pm 2$ kpc, $n = 5.4 \pm 1.8$ and $r_{eff} = 7 \pm 3$ kpc. The Einasto profile with an Osipkov-Merritt flattening (Eqn. 8) fits well to the data with $q_{inf} = 0.96 \pm 0.05$, $q_0 = 0.2 \pm 0.1$, $r_0 = 15 \pm 3$ kpc, $n = 4.6 \pm 1.5$ and $r_{eff} = 8 \pm 3$ kpc. When the flattening follows the Sluis-Arnold form (Eqn. 9), the best-fit Einasto profile has $q_0 = 0.3 \pm 0.1$, $r_0 = 6 \pm 3$ kpc, $n = 4.2 \pm 1.5$ and $r_{eff} = 8 \pm 3$ kpc. The best-fitting models indicate that the stellar halo is very flat at the center, but becomes nearly spherical at larger radii. We compare the three best-fit models of the flattening variation, and find they are consistent with each other (Figure 8). Compared to the stellar halo with no change of shape, the slope of the density profile will vary slower ($n \sim 5$ *vs.* $n = 2.2$), but the distribution of mass is more concentrated ($r_{eff} \sim 8$ kpc *vs.* $r_{eff} = 21$ kpc), when the stellar halo changes from a flattened distribution at smaller radii to an almost spherical distribution at larger radii.

We have fitted a set of models with constant or variable flattening, and Figure 5 shows all models fit well with the data. However, it can not reflect the difference between these models. So, we will explore it in §4.5.

4.5. The model comparisons

Our best-fitting density distributions can be used to estimate the mass M(< r) within a radius r and the total mass of the Milky Way through Jeans model. According to Jeans equation, $\frac{\mathrm{dln}\nu}{\mathrm{dlnr}}$[2] plays an important role when calculating M(< r), so we explore the difference between our best-fitted models by comparing their $\frac{\mathrm{dln}\nu}{\mathrm{dlnr}}$. The stellar halo is oblate, so the density profile is axisymmetric. The spherical $\frac{\mathrm{dln}\nu}{\mathrm{dlnr}}$ can not reflect the difference caused by the flattening. Therefore, we use $\frac{\mathrm{dln}\nu(\mathrm{R},\mathrm{R}/\sqrt{2})}{\mathrm{dlnR}}$ in the direction along the diagonal line in (x, y, z) coordinate to do the comparison. Comparing all models in one plot will make the figure unreadable, so we compare the Einasto profiles with different forms of flattening variation firstly. The upper panel of Figure 9 shows all three forms of flattening reach consistent density profiles. Since the Einasto profiles with different definitions of flattening variation are consistent, we will only use one of them to compare with the models with constant flattening. Figure 9 (lower panel) shows the consistency between the models with constant or variable flattening.

5. Discussion

We use the dominated part of the SEGUE-2 K giants, "l-color K giants", to derive the underlying stellar distribution accounting for the selection function of the data. The "selection biases" of SEGUE-2 l-color K giants are explored by the comparison between the distribution of successfully spectroscopic targets and the complete parent set of photometric targets in color-magnitude plane. We find the selection function is independent on color and magnitude, and as simple as a plate-dependent fraction. After that, we apply the plate-dependent selection function to l-color K giants, and the best stellar density profiles are identified by the maximum-likelihood approach.

Based on the data with 10 kpc $< \mathrm{r_{gc}} <$ 80 kpc and $-3.5 <$ [Fe/H] < -1.2, we find the stellar halo is oblate, and its shape depends strongly on the metallicity. Our best-fitting models suggest a flattening of $\mathrm{q} = 0.78 \pm 0.02$, and a steeper profile at larger radii. We prefer

[2]The $\frac{\mathrm{dln}\nu}{\mathrm{dlnr}}$ indicates the steepness of the density profile.

to using Einasto profile to represent the stellar halo density as:

$$\nu_\star(\mathrm{r_q}) \;\propto\; exp\left\{-6.27\left[(r_q/21)^{1/2.2}-1\right]\right\}, \text{with } \mathrm{r_q}=\sqrt{\mathrm{R}^2+\mathrm{z}^2/0.78^2}. \tag{10}$$

Meanwhile, the broken power-law is also an equally good law for the stellar halo density. SEGUE-2 l-color K giants are consistent with a broken power-law with an inner slope of 2.7 and an outer slope of 4.2, the break radius at 30kpc, which can be expressed as:

$$\nu_\star\left(\mathrm{r_q}\right) \propto \begin{cases} \mathrm{r_q}^{-2.7}, & \mathrm{r_q} \leq 30 \text{ kpc} \\ \mathrm{r_q}^{-4.2}, & \mathrm{r_q} > 30 \text{ kpc} \end{cases} \tag{11}$$

These two formulae are fundamental results for the stellar density models with a constant flattening in our paper. The results are qualitatively similar to those obtained by Sesar et al. (2011) using photometric main-sequence stars and Deason et al. (2011) using photometric A-type stars, but quantitatively different from them. Furthermore, we find the evidence for the variation of flattening with distance, which confirms the finding of Preston et al. (1991), but is inconsistent with findings of Sluis & Arnold (1998); Sesar et al. (2011); Deason et al. (2011)

In summary, we find the SEGUE-2 l-color K giants are well described by an oblate density distribution with a constant flattening of q $\sim$ 0.78 and a steeper profile at larger radii. In addition, we find the evidence of the variation of flattening. Comparing to previous studies, our findings indicate the stellar halo is not as flat as Sesar et al. (2011, ;q=0.7) and Deason et al. (2011, ;q=0.58), and the radial distribution of the density profile is consistent with Sesar et al. (2011), but is not as steep as Deason et al. (2011, 2014).

Similar to the comparisons in §4.5, we plotted $\frac{\mathrm{dln}\nu(\mathrm{R},\mathrm{R}/\sqrt{2})}{\mathrm{dlnR}}$ for the best-fit density profiles of Deason et al. (2011, 2014) over our preferred models shown as Figure 10. Deason et al. (2011, 2014) found much steeper density distribution of the stellar halo.

We have applied our best-fit stellar density profiles and the radial velocity dispersion of the SEGUE K giants to the axisymmetric Jeans model to estimate the total mass of the Milky Way by assuming the gravity potential model, and get the total mass of $\mathrm{M_{340}} = 1.3 \pm 0.3 \times 10^{12}\mathrm{M_\odot}$ (see Büdenbender et al. 2015 for details).

Funding for SDSS-III has been provided by the Alfred P. Sloan Foundation, the Participating Institutions, the National Science Foundation, and the U.S. Department of Energy Office of Science. The SDSS-III web site is http://www.sdss3.org/.

SDSS-III is managed by the Astrophysical Research Consortium for the Participating Institutions of the SDSS-III Collaboration including the University of Arizona, the Brazilian

Participation Group, Brookhaven National Laboratory, University of Cambridge, Carnegie Mellon University, University of Florida, the French Participation Group, the German Participation Group, Harvard University, the Instituto de Astrofisica de Canarias, the Michigan State/Notre Dame/JINA Participation Group, Johns Hopkins University, Lawrence Berkeley National Laboratory, Max Planck Institute for Astrophysics, Max Planck Institute for Extraterrestrial Physics, New Mexico State University, New York University, Ohio State University, Pennsylvania State University, University of Portsmouth, Princeton University, the Spanish Participation Group, University of Tokyo, University of Utah, Vanderbilt University, University of Virginia, University of Washington, and Yale University.

This work was made possible by the support of the Max-Planck-Institute for Astronomy, and supported by the National Natural Science Foundation of China under grant Nos. 11103031, 11233004, 11390371 and 11003017, and supported by the Young Researcher Grant of National Astronomical Observatories, Chinese Academy of Sciences. This paper was partially supported by the DFG's SFB-881 grant 'The Milky Way System'.

X.-X. Xue acknowledges the Alexandra Von Humboldt foundation for a fellowship

REFERENCES

Ahn, C. P., Alexandroff, R., Allende Prieto, C., et al. 2012, ApJS, 203, 21

Bovy, J., Rix, H.-W., Liu, C., et al. 2012, ApJ, 753, 148

De Propris, R., Harrison, C. D., & Mares, P. J. 2010, ApJ, 719, 1582

Deason, A. J., Belokurov, V., & Evans, N. W. 2011, MNRAS, 416, 2903

Deason, A. J., Belokurov, V., Koposov, S. E., & Rockosi, C. M. 2014, ApJ, 787, 30

Einasto, J. & Haud, U. 1989, A&A, 223, 89

Eisenstein, D. J., Weinberg, D. H., Agol, E., et al. 2011, AJ, 142, 72

Foreman-Mackey, D., Hogg, D. W., Lang, D., & Goodman, J. 2013, PASP, 125, 306

Fukugita, M., Ichikawa, T., Gunn, J. E., et al. 1996, AJ, 111, 1748

Gould, A., Flynn, C., & Bahcall, J. N. 1998, ApJ, 503, 798

Graham, A. W., Merritt, D., Moore, B., Diemand, J., & Terzić, B. 2006, AJ, 132, 2711

Gunn, J. E., Carr, M., Rockosi, C., et al. 1998, AJ, 116, 3040

Harris, W. E. 1976, AJ, 81, 1095

Hawkins, M. R. S. 1984, MNRAS, 206, 433

Jeans, J. H. 1915, MNRAS, 76, 70

Lee, Y. S., Beers, T. C., Allende Prieto, C., et al. 2011, AJ, 141, 90

Lee, Y. S., Beers, T. C., Sivarani, T., et al. 2008a, AJ, 136, 2022

Lee, Y. S., Beers, T. C., Sivarani, T., et al. 2008b, AJ, 136, 2050

Merritt, D., Graham, A. W., Moore, B., Diemand, J., & Terzić, B. 2006, AJ, 132, 2685

Navarro, J. F., Ludlow, A., Springel, V., et al. 2010, MNRAS, 402, 21

Pier, J. R., Munn, J. A., Hindsley, R. B., et al. 2003, AJ, 125, 1559

Preston, G. W., Shectman, S. A., & Beers, T. C. 1991, ApJ, 375, 121

Rix, H.-W. & Bovy, J. 2013, A&A Rev., 21, 61

Robin, A. C., Reylé, C., & Crézé, M. 2000, A&A, 359, 103

Saha, A. 1985, ApJ, 289, 310

Sérsic, J. L. 1963, Boletin de la Asociacion Argentina de Astronomia La Plata Argentina, 6, 41

Sesar, B., Jurić, M., & Ivezić, Ž. 2011, ApJ, 731, 4

Siegel, M. H., Majewski, S. R., Reid, I. N., & Thompson, I. B. 2002, ApJ, 578, 151

Sluis, A. P. N. & Arnold, R. A. 1998, MNRAS, 297, 732

Sommer-Larsen, J. 1987, MNRAS, 227, 21P

Soubiran, C. 1993, A&A, 274, 181

Stoughton, C., Lupton, R. H., Bernardi, M., et al. 2002, AJ, 123, 485

Wetterer, C. J. & McGraw, J. T. 1996, AJ, 112, 1046

Xue, X.-X., Ma, Z., Rix, H.-W., et al. 2014, ApJ, 784, 170

Xue, X.-X., Rix, H.-W., Yanny, B., et al. 2011, ApJ, 738, 79

Yanny, B., Rockosi, C., Newberg, H. J., et al. 2009, AJ, 137, 4377

York, D. G., Adelman, J., Anderson, Jr., J. E., et al. 2000, AJ, 120, 1579

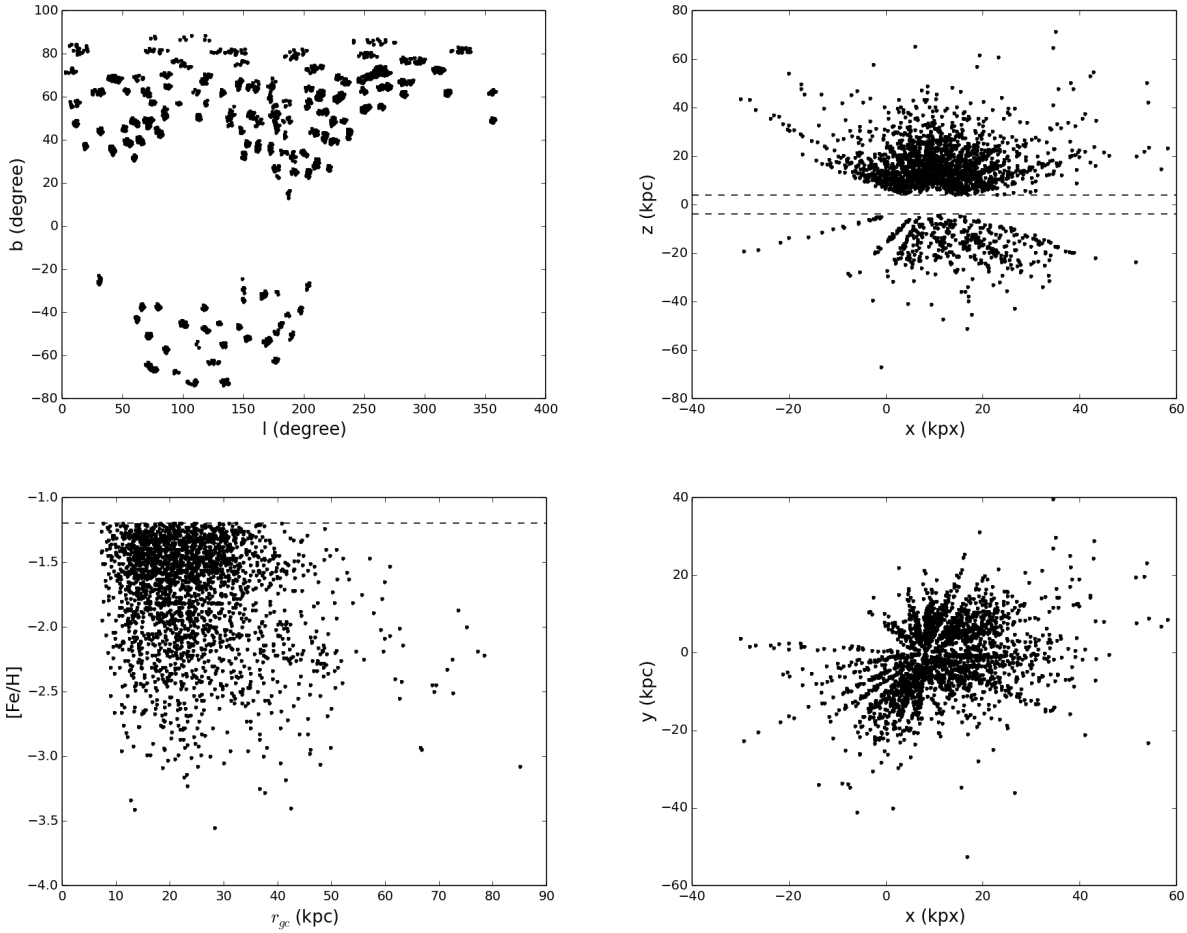

Fig. 1.—: (Upper left) The sky coverage and the spatial distributions (right panel) of SEGUE-2 l-color K giants appear to be pencil-beam due to the nature of SEGUE survey. (Lower left) The distribution of metallicities along with the Galactocentric radii shows the mean metallicity is about -1.75 dex, and some K giants have metallicities of ~ -3.5. The stars with [Fe/H] > -1.2 and |z| < 4 kpc are culled because they could belong to the disk.

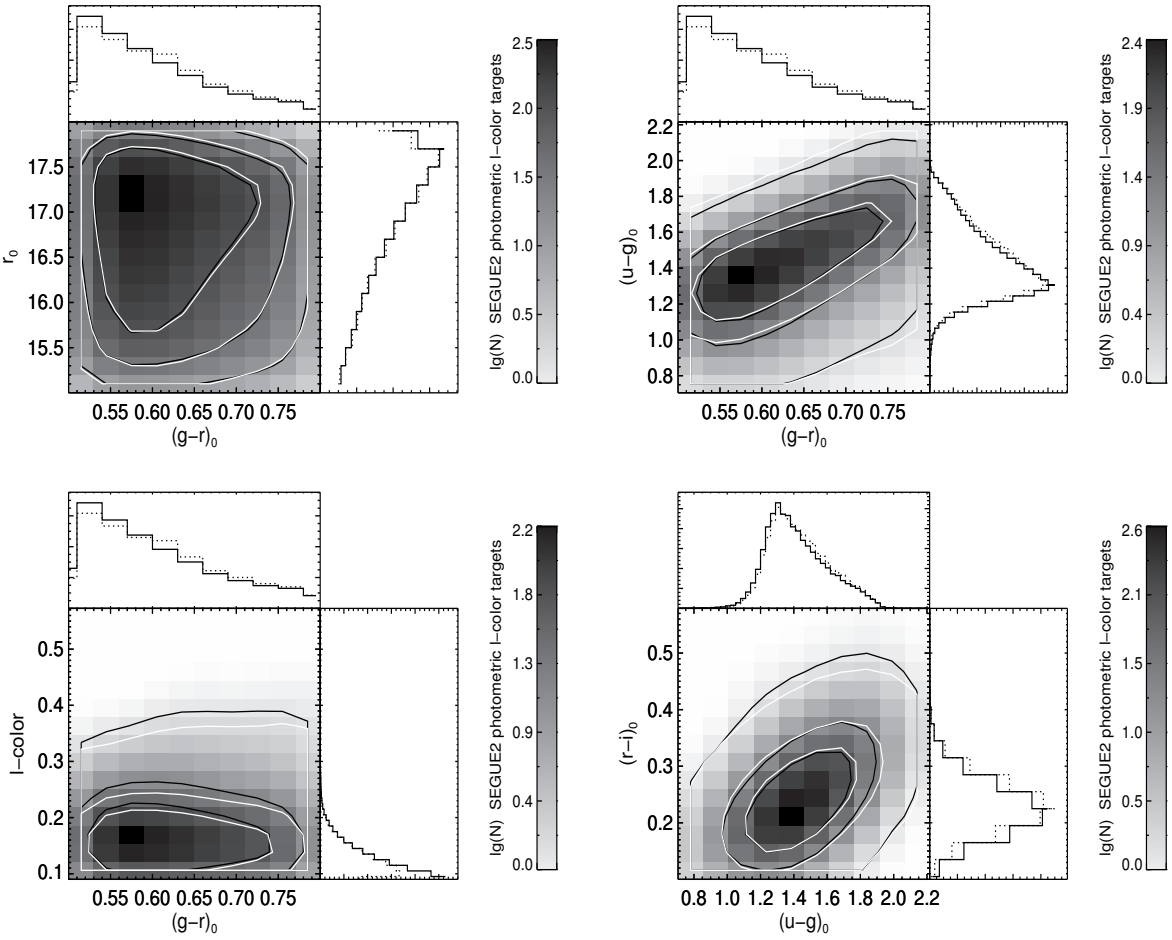

Fig. 2.—: Distribution of SEGUE-2 photometric l-color K-giant candidates (gray map, black contours, solid histogram) and the successfully spectroscopic sample (white contours, dotted histogram). The contours contain 68%, 95% and 99% of the distribution. The spectroscopic sampling is relatively fair in colors and magnitudes.

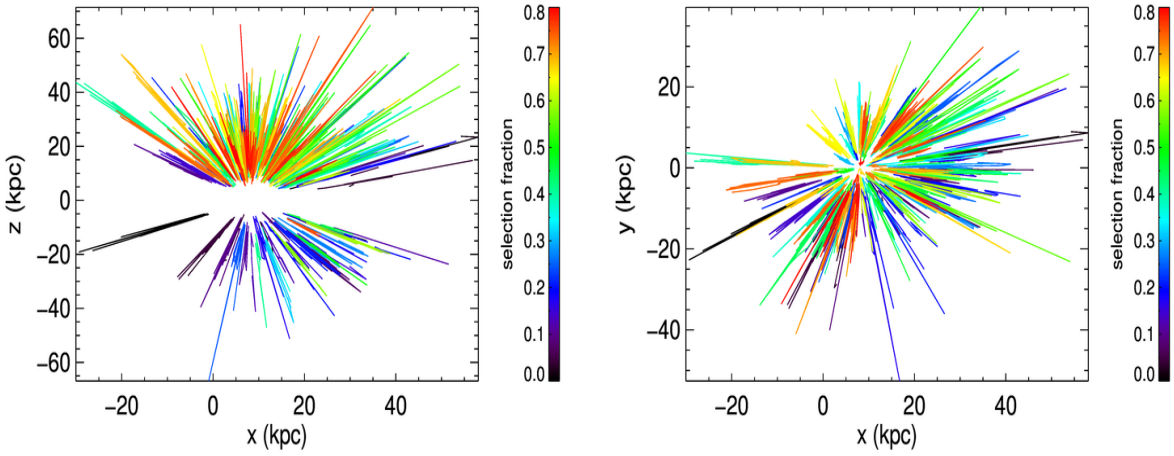

Fig. 3.—: The SEGUE-2 selection function of l-color K giants, as a function of Galactic coordinates X and Y (left panel), and of Galactocentric coordinates X and vertical height Z (right panel).

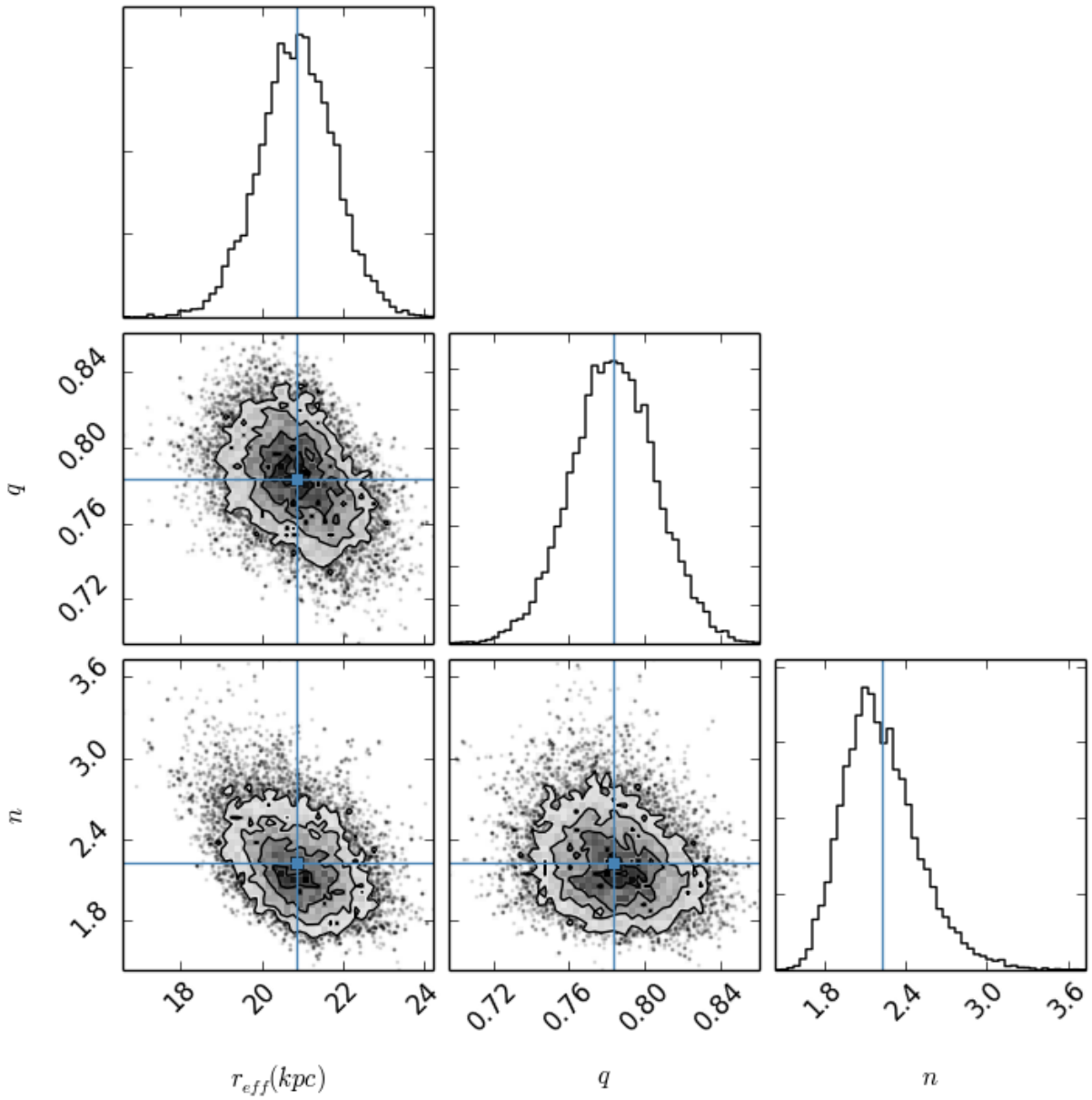

Fig. 4.—: The triangle plot shows all the one and two dimensional projections of the posterior probability distributions of parameters $(\mathrm{q}, \mathrm{n}, \mathrm{r_{eff}})$ of Einasto profile. The blue lines and squares mark the best value of each parameter.

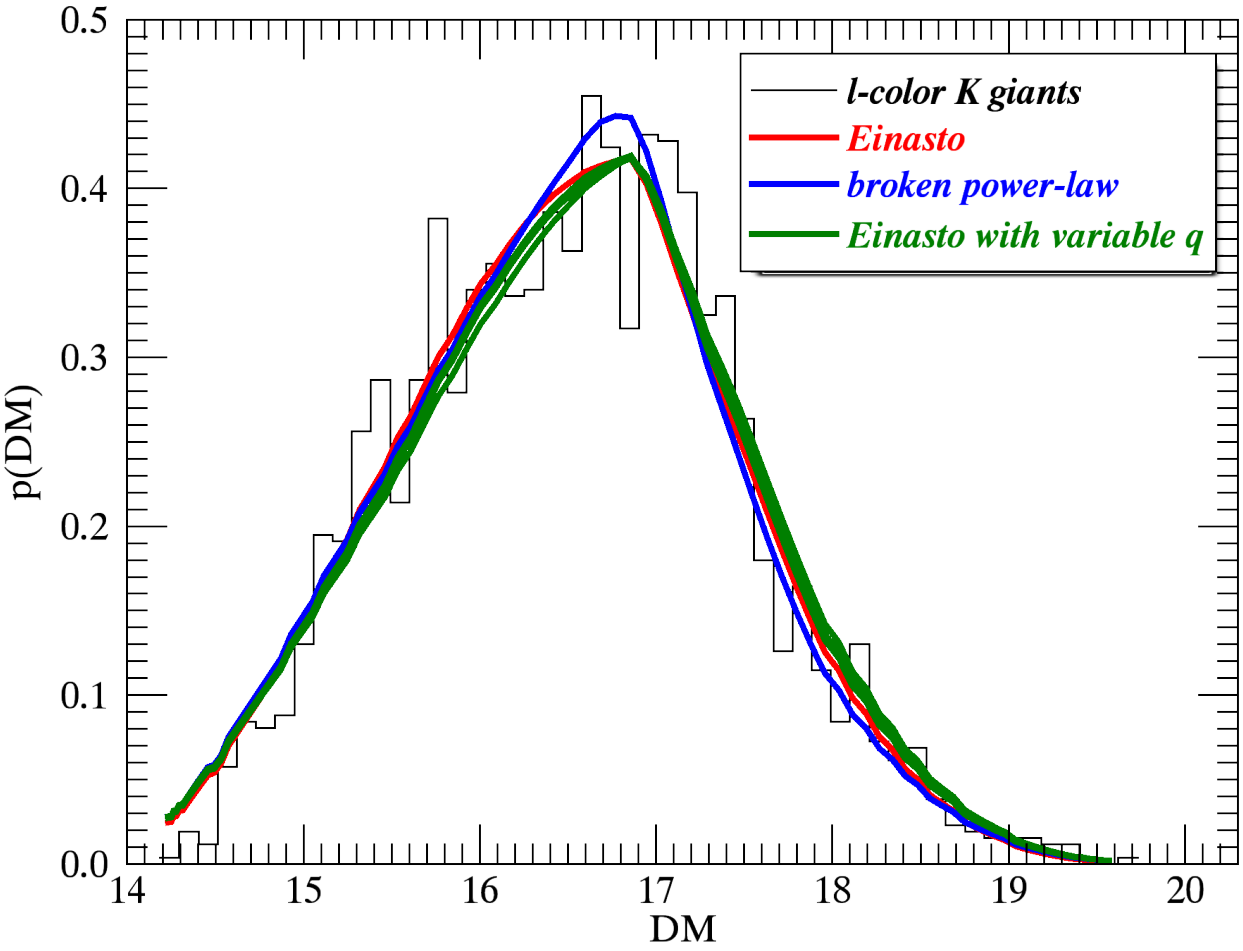

Fig. 5.—: The comparison between the observed distance-modulus distribution and the predicted distributions by the best-fitting models. All of the best-fitting models fit well.

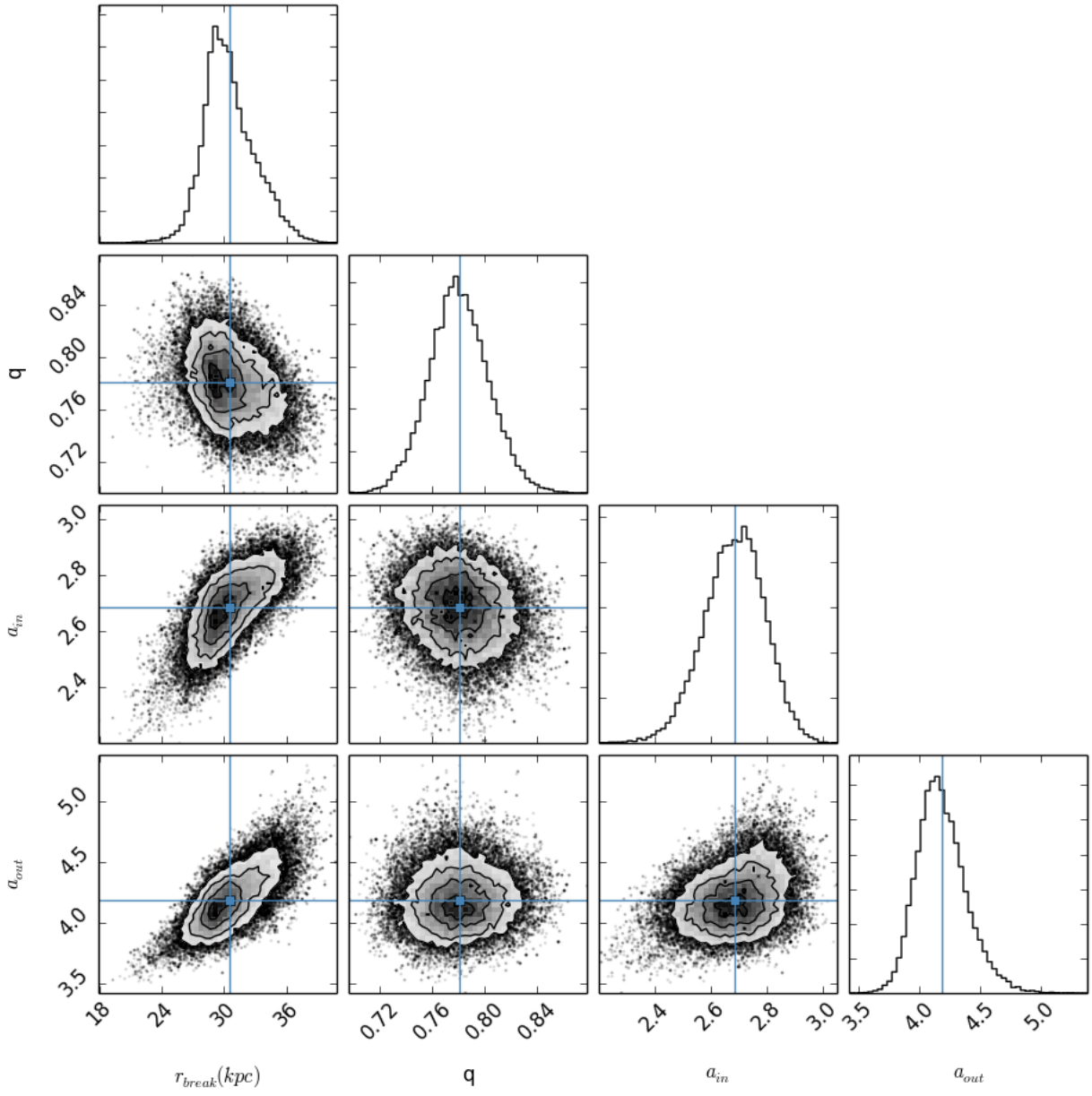

Fig. 6.—: The triangle plot shows all the one and two dimensional projections of the posterior probability distributions of parameters ($\mathrm{q}, \alpha_{\mathrm{in}}, \alpha_{\mathrm{out}}, \mathrm{r}_{\mathrm{break}}$) of the broken power-law profile. The blue lines and squares mark the best value of each parameter.

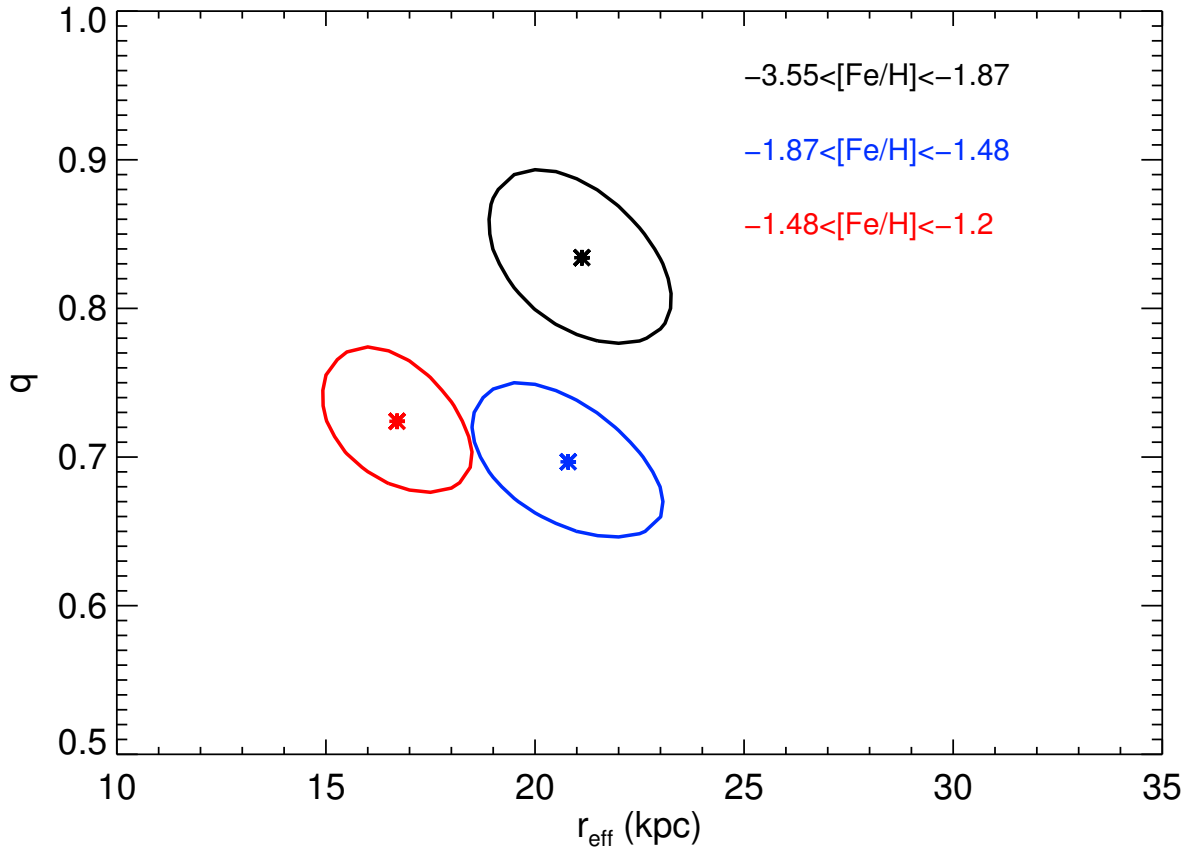

Fig. 7.—: The best-fit values of flattening and effective radii and their 68% confidence levels for three sub-samples in different metallicity bins. The shape of the stellar halo has strong dependence on the metallicity, while the radial profile is independent on metallicity.

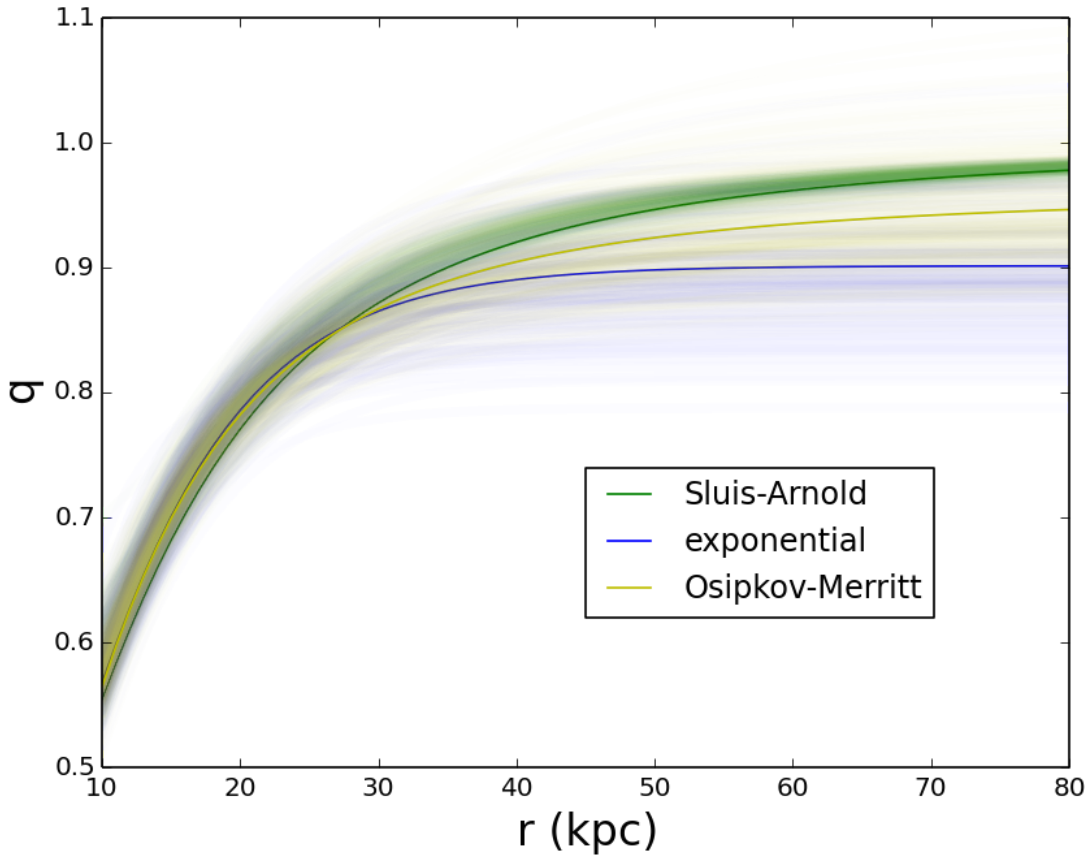

Fig. 8.—: The comparison between three models of flattening variation. They are consistent with each other.

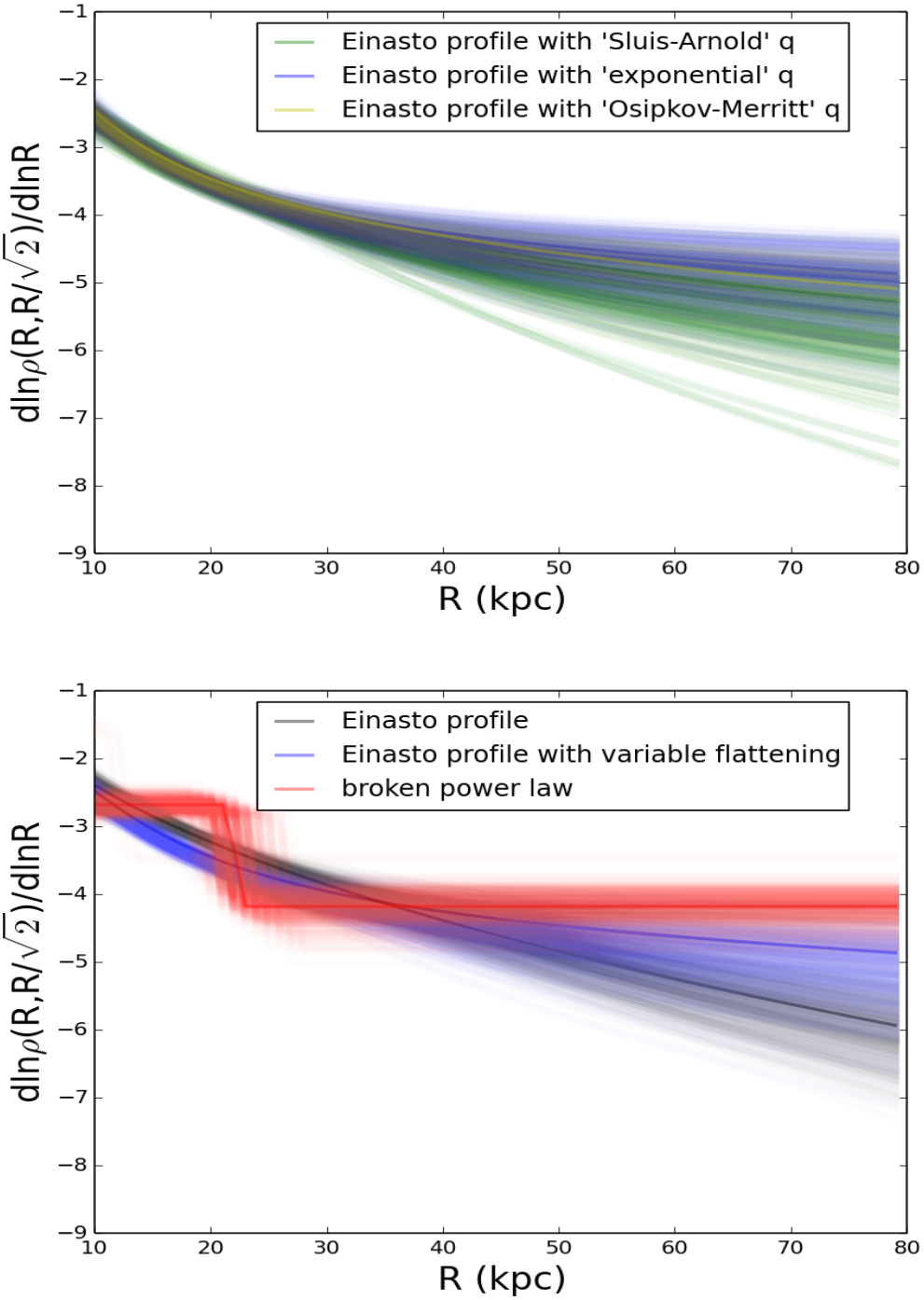

Fig. 9.—: (Upper panel) $\frac{\mathrm{dln}\nu(\mathrm{R},\mathrm{R}/\sqrt{2})}{\mathrm{dlnR}}$ for best-fit Einasto profiles with different definitions of flattening variation. (Lower panel) $\frac{\mathrm{dln}\nu(\mathrm{R},\mathrm{R}/\sqrt{2})}{\mathrm{dlnR}}$ for best-fit broken power-law with constant flattening (red) and best-fit Einasto profiles with constant flattening (black) or variable flattening (blue).

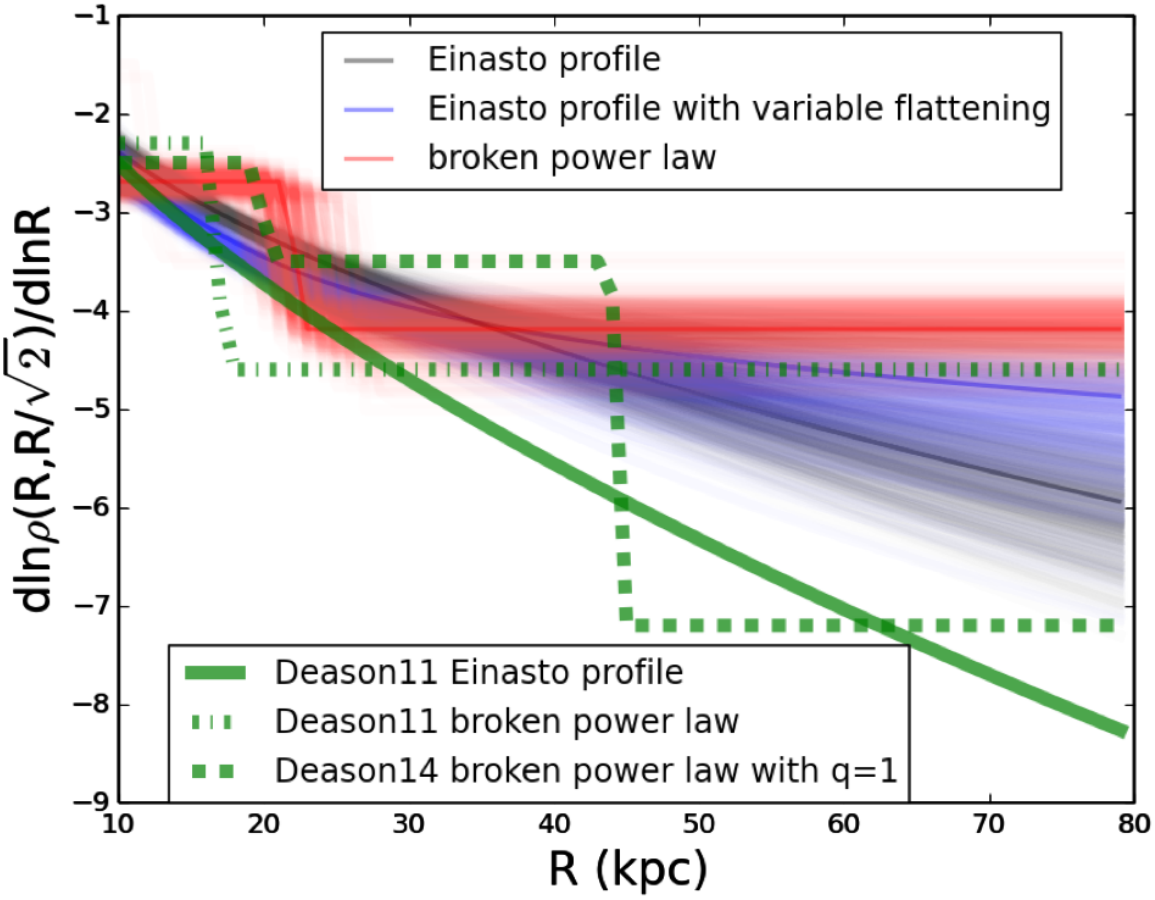

Fig. 10.—: $\frac{\mathrm{dln}\nu(\mathrm{R},\mathrm{R}/\sqrt{2})}{\mathrm{dlnR}}$ for our best-fit broken power-law with constant flattening (red) and best-fit Einasto profiles with constant flattening (black) or variable flattening (blue) and the best-fit models of Deason et al. (2011, 2014, green).